The Aeronautical Journal (2023), **127**, pp. 773–795
doi:10.1017/aer.2022.88

REGULAR PAPER

Optimisation design of turbofan engine using infrared stealth technology

M. Chen* , H. Chen , H. Zhang and J. Luo

Nanjing University of Aeronautics and Astronautics, Nanjing, Jiangsu, China
*Corresponding author. Email: 1358025658@qq.com

Received: 28 January 2022; **Revised:** 13 May 2022; **Accepted:** 7 October 2022

Keywords: Turbofan; infrared; Optimization; Stealth

Abstract

To obtain the optimal solution for the performance of the turbofan engine using infrared stealth technology, an engine mathematical model with a backward infrared radiation intensity calculation module was established. The effects of infrared suppression measures on the performance of turbofan engines were analysed. Based on the multi-objective particle swarm optimisation (MOPSO) algorithm, the optimal solution for the performance in the cruise state of the reference engine refitted with the infrared radiation suppression module was obtained; Further, through the multiple design points (MDPs) concept, the thermal cycle optimisation design of the turbofan engine was carried out. The results show that the integrated fully shielded guiding strut (IFSGS) with air film cooling had the ideal infrared suppression effect. Compared with the reference engine refitted with infrared radiation suppression module, the engine after cycle optimisation design could obtain better infrared stealth performance.

Nomenclature

C_8	the area ratio of the nozzle throat
C_9	the area ratio of the nozzle exit
F	engine thrust
IR	infrared radiation intensity
m_c	mass flow of cooling air flowing through the IFSGS
m_w	mass flow of cooling air flowing through the nozzle expansion section
M_6	mixer entry Mach number
M_{br}	blowing ratio
sfc	specific fuel consumption rate
T_{t4}	burner exit total temperature
W	air intake
α	bypass ratio
ε_c	cooling airflow fractions of the IFSGS
ε_w	cooling airflow fractions of the nozzle expansion section
η_c	film cooling efficiency
π_C	compressor pressure ratio
π_F	fan pressure ratio
π_T	total pressure ratio

Subscripts

CR	cruise state
$CR1$	subsonic cruise state
$CR2$	supersonic cruise state
TO	ground state

1.0 Introduction

The rapid development of infrared detection and guidance technology in recent years has brought severe challenges to the survivability of aircraft on the battlefield. In various local wars in recent years, the number of targets shot down by infrared guided missiles has reached three times that of radar guided missiles [1]. Facing the serious threat of infrared detection systems and infrared guided missiles, it is imperative to research the infrared stealth technology of aircraft.

The turbofan engine is the main power source of active combat aircraft, and its exhaust system is an important infrared radiation source. When the flight Mach number of aircraft is low (less than 1.6 Mach), the proportion of infrared radiation of the exhaust system can reach more than 90% of the total infrared radiation of aircraft in the medium band of 3–5μm [2]. The infrared radiation of the exhaust system mainly comes from the high-temperature solid wall and the high-temperature gas. In the rear of the aircraft, the infrared radiation of high-temperature solid walls accounts for more than 70% of the total radiation. It can be seen that the development of engine infrared stealth technology is of great significance to reduce the infrared characteristics of aircraft [3, 4].

The infrared characteristics of the engine are reflected from the exhaust system, but the stealth of the engine is not only related to the exhaust system but also related to the overall design of the engine and aircraft. The realisation of infrared stealth will affect the cycle design. Only by modifying the exhaust system of an active turbofan is difficult to achieve the optimal infrared stealth performance. This is because the unalterable constraints such as the body structure and thermal cycle parameters limit the application of many efficient infrared suppression measures, which greatly restricts the comprehensive infrared stealth effect.

The research shows that the infrared radiation characteristics of the engine can be effectively reduced by shielding and cooling the high-temperature components in the exhaust system [5–12]. However, the cooling gas needs to be drawn from other parts of the engine, which will inevitably affect the overall performance, resulting in reduced thrust and increased fuel consumption. The shielding of high-temperature components requires the alteration of the exhaust system structure, which is bound to have an impact on the aerodynamic performance. Therefore, the installation of a bleed air cooling device on a designed engine may make it unable to meet the original performance requirements. In other words, to reduce the infrared radiation characteristics of turbofan engines as much as possible, the impact of infrared suppression measures must be fully considered in the overall design process, and a new low-infrared engine has to be designed [6]. However, the existing turbofan engines do not consider infrared stealth in the overall design process.

The traditional aero-engine cycle design applies the single design point (SDP) concept [13–15]. The specific method is to first determine the cycle parameters of the design point to ensure that the performance of the design point meets the requirements, and then evaluate the performance of the engine at the off-design points. If the performance of the off-design points does not meet the requirements, reformulate the cycle parameters of the design point, so as to repeat the progress, until the performance of the design point and off-design points meet the requirements. The multiple design points (MDPs) method is a more novel engine cycle design concept [16–20]. It combines the design parameters of the traditional design point (aerodynamic design point) with off-design points. Multiple typical working states can be taken as design points, and the performance requirements and constraints at all design points will be included in the equations to be solved. Finally, a set of feasible design parameters meeting the requirements of all design points are solved. The cycle design of a turbofan engine using infrared stealth technology is more suitable for the MDPs concept because not all flight states need infrared feature suppression. For example, in the takeoff state, thrust is the most important performance requirement, and infrared suppression is not required. For the combat state of the afterburner, the infrared characteristics are doubled and cannot be effectively suppressed. In the cruise state, the infrared characteristics and the fuel consumption rate should be considered at the same time. It can be seen that the overall design of turbofan engines using infrared stealth technology is essentially a multi-constraint and multi-objective optimisation problem.

https://doi.org/10.1017/aer.2022.88 Published online by Cambridge University Press

Table 1. *Definition of engine sections*

Section number	Section definition
1	Air entry
2	Fan entry
2.5	LP compressor exit & HP compressor entry
13	Fan exit
3	HP compressor exit
3.1	Burner entry
4	Burner exit & HP turbine guide entry
4.1	HP turbine guide exit & HP turbine entry
4.4	HP turbine exit & LP turbine guide entry
4.5	LP turbine guide exit & LP turbine entry
5	LP turbine exit
15	Bleed position of the bypass duct
6	Core stream mixer entry
16	Fan bypass stream mixer entry
IFSGS	Integrated fully shielded guiding strut
6A	Mixer exit & afterburner entry
7	Afterburner exit & nozzle entry
8	Nozzle throat
9	Nozzle exit

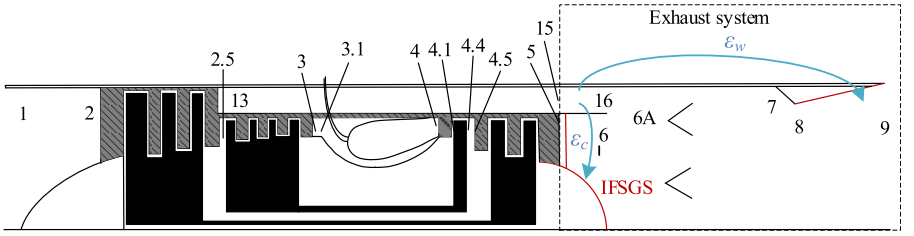

Figure 1. *Turbofan engine using infrared stealth technology.*

Taking a small bypass ratio turbofan engine without infrared stealth capability as the reference model, this paper studied the optimal performance boundary of the reference model in cruise state after refitting with an infrared suppression module. Further, based on the MDPs concept, taking the thrust in the ground state, the specific fuel consumption rate, and infrared radiation intensity in the cruise state as the optimisation objectives, the MOPSO algorithm [21] was used to optimise the overall performance of the turbofan engine, and compared with the reference engine refitting with infrared suppression module.

2.0 Turbofan engine model using infrared stealth technology

2.1 Aerodynamic performance calculation

The turbofan engine model is shown in Fig. 1, in which the section numbers are defined in Table 1. The mathematical model used in this paper includes the following basic assumptions:

(1) The total pressure recovery coefficient of the burner, afterburner, and nozzle remained unchanged.

(2) The percentage of high and low-pressure turbine blade cooling gas in the total airflow of the engine remained unchanged, and the power separation remains unchanged, ignoring the air leakage.

https://doi.org/10.1017/aer.2022.88 Published online by Cambridge University Press

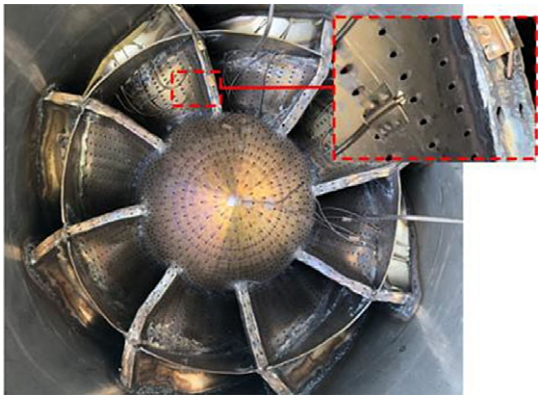

Figure 2. *IFSGS with air film holes*[5].

Figure 3. *Air film holes on nozzle surface of F119 engine*[5].

(3) It was assumed that the internal flow of the engine was a quasi-one-dimensional ideal gas, and its specific heat changed with gas temperature and fuel-air ratio.

(4) Except the throat area and exit area of the nozzle, the other cross-sectional area of the engine was constant.

Behind the exhaust system, the infrared radiation at the exit of the low-pressure turbine, central cone, and the inner surface of the nozzle expansion section accounts for a large proportion. The targeted infrared suppression measure is to install the integrated fully shielded guiding strut (IFSGS) at the exit of the low-pressure turbine. The IFSGS integrates the guiding strut and the central cone, which makes the low-pressure turbine rotor completely invisible behind the engine. The IFSGS is hollow inside to pass cooling airflow. The air film cooling method was applied to the IFSGS (Fig. 2) and the inner surface of the nozzle expansion section (Fig. 3). The cooling air flows into the mainstream of the exhaust system through the densely packed tiny holes.

Considering the requirements of accuracy and real-time ability, the component level model of the engine was adopted, that is, first establish the model of each component according to the principle of aerodynamic thermodynamics and characteristic diagram of rotor components, and then integrate all single components into a complete engine mathematical model according to the matching relationship between each component, which can be expressed by the following six equations:

HP rotor power balance equation:

$$E_{q1} = \frac{H_{PT}}{H_{PC}/\eta_{mH} + H_{PEXT}/\eta_P} - 1 \tag{1}$$

https://doi.org/10.1017/aer.2022.88 Published online by Cambridge University Press

where H_{PT} is the power generated by the HP turbine, H_{PC} is the power consumed by the compressor, H_{PEXT} is the shaft power extraction of the HP turbine, η_{mH} is the mechanical efficiency of the HP shaft, and η_P is the power extraction efficiency.

LP rotor power balance equation:

$$E_{q2} = \frac{H_{PL}}{H_{PF}/\eta_{mL}} \tag{2}$$

where H_{PL} is the power generated by the LP turbine and H_{PF} is the power consumed by the fan, η_{mL} is the efficiency of the LP shaft.

HP turbine inlet flow continuity equation:

$$E_{q3} = \frac{W_{g4c}}{W_{g41c}} - 1 \tag{3}$$

where W_{g4c} is the inlet flow of the HP turbine and W_{g41c} is the outlet flow of the combustion chamber.

LP turbine inlet flow continuity equation:

$$E_{q4} = \frac{W_{g41c}}{W_{g45c}} - 1 \tag{4}$$

where W_{g45c} is the inlet flow of the LP turbine.

Static pressure balance equation at the entry of the mixer:

$$E_{q5} = \frac{P_6}{P_{16}} - 1 \tag{5}$$

where P_6 is the core stream static pressure, and P_{16} is the bypass stream static pressure.

Total pressure balance equation at the tail nozzle throat:

$$E_{q6} = \frac{P_{t8c}}{P_{t8}} - 1 \tag{6}$$

where P_{t8c} is the total pressure calculated according to the nozzle flow, and P_{t8} is the total pressure at the outlet of the tail nozzle calculated according to the incoming flow.

Two cooling air streams with a mass flow of m_c and m_w are led out from the bypass duct to cool the surface of the IFSGS and the nozzle expansion section respectively. The cooling airflow fractions ε_c and ε_w are defined as follows:

$$\varepsilon_c = \frac{m_c}{m_3} \tag{7}$$

$$\varepsilon_w = \frac{m_w}{m_3} \tag{8}$$

where m_c and m_w respectively represent the mass flow of cooling air flowing through the IFSGS and nozzle expansion section; m_3 is the air mass flow at the HP compressor exit. The residuals of the balance equations are affected by the cooling airflow fractions.

When the high-temperature wall is cooled, its surface temperature can be obtained by the following formula:

$$\eta_c = \frac{T_m - T_f}{T_m - T_{cool}} \tag{9}$$

where η_c is the film cooling efficiency, T_m is the mainstream temperature; T_f is the wall temperature; T_{cool} is the cooling air temperature.

The blowing ratio M_{br} of the high-temperature wall is defined as follows:

$$M_{br} = \frac{\rho_c V_c}{\rho_m V_m} \tag{10}$$

where ρ_c and V_c are the density and velocity of the cooling air; ρ_m and V_m are the density and velocity of the mainstream.

https://doi.org/10.1017/aer.2022.88 Published online by Cambridge University Press

The film cooling efficiency η_c is a function of the blowing ratio M_{br}, and the form of the function is determined by the size and arrangement of the air film holes. The empirical formula used in this paper is:

$$\eta_c = 0.6672 \cdot \left(e^{-0.01156 M_{br}} - e^{-52.79 M_{br}}\right) \tag{11}$$

When the control parameters (fuel flow rate, nozzle area, bleed air flow rate, etc.) of the engine is given, the Newton-Raphson method can be used to solve the balance equations. For the above six balance equations, the corresponding six unknowns are HP rotor speed n_H, LP rotor speed n_L, fan pressure ratio π_F, compressor pressure ratio π_C, HP turbine pressure ratio π_{HT}, LP turbine pressure ratio π_{HL}, so the balance equations can be expressed as the function of the six unknowns, and the system of equations to be solved is:

$$F(X) = \begin{cases} E_{q1}(n_H, n_L, \pi_F, \pi_C, \pi_{HT}, \pi_{LT}) = 0 \\ E_{q2}(n_H, n_L, \pi_F, \pi_C, \pi_{HT}, \pi_{LT}) = 0 \\ \vdots \\ E_{q6}(n_H, n_L, \pi_F, \pi_C, \pi_{HT}, \pi_{LT}) = 0 \end{cases} \tag{12}$$

where, $X = [n_H \quad n_L \quad \pi_F \quad \pi_C \quad \pi_{HT} \quad \pi_{LT}]^T$. X will be iteratively computed until the residuals of the balance equations are less than 10^{-6}. The iteration formula of X is:

$$X^{n+1} = X^n - [F'(X^n)]^{-1} F(X^n) \tag{13}$$

$$F'(X^n) = \begin{bmatrix} \frac{\partial E_{q1}}{\partial n_H} & \frac{\partial E_{q1}}{\partial n_L} & \frac{\partial E_{q1}}{\partial \pi_F} & \frac{\partial E_{q1}}{\partial \pi_C} & \frac{\partial E_{q1}}{\partial \pi_{HT}} & \frac{\partial E_{q1}}{\partial \pi_{LT}} \\ \frac{\partial E_{q2}}{\partial n_H} & \frac{\partial E_{q2}}{\partial n_L} & \frac{\partial E_{q2}}{\partial \pi_F} & \frac{\partial E_{q2}}{\partial \pi_C} & \frac{\partial E_{q2}}{\partial \pi_{HT}} & \frac{\partial E_{q2}}{\partial \pi_{LT}} \\ \vdots & \vdots & \vdots & \vdots & \vdots & \vdots \\ \frac{\partial E_{q6}}{\partial n_H} & \frac{\partial E_{q6}}{\partial n_L} & \frac{\partial E_{q6}}{\partial \pi_F} & \frac{\partial E_{q6}}{\partial \pi_C} & \frac{\partial E_{q6}}{\partial \pi_{HT}} & \frac{\partial E_{q6}}{\partial \pi_{LT}} \end{bmatrix} \tag{14}$$

The aerodynamic and thermodynamic parameters of each section and the overall performance parameters of the engine can be further obtained when the equations are solved. The formula of the engine thrust is:

$$F = W_9(V_9 - V_0) + (P_{s9} - P_{s0})A_9 \tag{15}$$

where W_9 is the flow rate at the nozzle exit, V_9 and V_0 are the gas velocity at the nozzle exit and the atmosphere; P_{s9} and P_{s0} are the gas static pressure at the nozzle exit and the atmosphere.

The specific fuel consumption rate is:

$$sfc = \left(W_f + W_{fAB}\right)/F \tag{16}$$

where W_f and W_{fAB} are the fuel flow rate of the main burner and the afterburner.

2.2 Calculation of backward infrared radiation intensity of exhaust system

After applying the infrared suppression measures described above, the high-temperature components that can be directly observed by the infrared detector in the backward direction of the turbofan engine exhaust system includes the IFSGS, the inner surface of the expansion section of the nozzle, and the part inner surface of bypass duct may also be observed. The infrared radiation of the exhaust system includes the infrared radiation of the high-temperature solid wall and the gas flow inside and outside the

https://doi.org/10.1017/aer.2022.88 Published online by Cambridge University Press

nozzle. The calculation method of the backward infrared radiation intensity of the exhaust system is as the function in reference 6:

$$IR = \frac{A_c \varepsilon_{I,c}}{\pi} \int_{\lambda} \sigma_\lambda M_{\lambda bb}(T_c)\, d\lambda + \frac{A_n \varepsilon_{I,n}}{\pi} \int_{\lambda} \sigma_\lambda M_{\lambda bb}(T_n)\, d\lambda + \frac{A_{16} \varepsilon_{I,16}}{\pi} \int_{\lambda} \sigma_\lambda M_{\lambda bb}(T_{16})\, d\lambda + I_{gas} \tag{17}$$

where, A_c, $\varepsilon_{I,c}$, T_c are the backward projected area, material emissivity, and surface temperature of the IFSGS respectively; A_n, $\varepsilon_{I,n}$, T_n are the backward projected area, material emissivity, and surface temperature of the expansion section of the nozzle respectively; A_{16}, $\varepsilon_{I,16}$, T_{16} are the backward projected area, material emissivity, and surface temperature of the visible inner surface of bypass duct respectively; $M_{\lambda bb}$ is the monochromatic radiance of blackbody; I_{gas} is the contribution value of gas radiation, and it is given as 8% of the total value of infrared radiation contribution of the solid wall according to experience; and σ_λ is the gas transmittance.

The infrared radiation energy of the exhaust system is mainly concentrated in the medium wave band, so the integral range of the wavelength is 3–5μm in the formula (17). At wavelength λ, the relationship between $M_{\lambda bb}$ and temperature T is determined by Planck's law, as shown in formula ((18)):

$$M_{\lambda bb}(T) = \frac{t_1}{\lambda^5} \cdot \frac{1}{e^{t_2/\lambda T} - 1} \tag{18}$$

where t_1 and t_2 are constants. $t_1 = (3.7415 \pm 0.0003) \times 10^{-16}$ (W·μm^4/m^2), $t_2 = (1.43879 \pm 0.00019) \times 10^{-2}$ (μm·K).

The formula of gas transmittance σ_λ is:

$$\sigma_\lambda = \prod_{1}^{i} (1 - \alpha_{\lambda,i}) \tag{19}$$

where the calculation formula of gas absorptivity $\sigma_{\lambda,i}$ (where i represents the microelement section on the centre line of the exhaust jet) is:

$$\alpha_{\lambda,i} = 1 - e^{-\kappa_{\lambda,i} \cdot \mathrm{d}x_i} \tag{20}$$

where $\mathrm{d}x_i$ represents the length of the microelement. The calculation formula of absorption coefficient $\kappa_{\lambda,i}$ is:

$$\kappa_{\lambda,i} = F_{CO_2,i} \cdot \frac{P_i \cdot 273}{1.01325 \times 10^5 \cdot T_i} \kappa^{STP}_{\lambda,CO_2}(T_i) + F_{H_2O,i} \cdot \frac{P_i \cdot 273}{1.01325 \times 10^5 \cdot T_i} \kappa^{STP}_{\lambda,H_2O}(T_i) \tag{21}$$

where $F_{CO2,i}$ and $F_{H2O,i}$ are mole fractions of carbon dioxide and water vapour in gas, respectively. P_i and T_i are pressure and temperature at section i, respectively. $\kappa^{STP}_{\lambda,CO_2}$ and $\kappa^{STP}_{\lambda,H_2O}$ are absorption coefficients of carbon dioxide and water vapour at standard temperature and pressure, respectively.

The empirical formula is applied to the temperature and component concentration change of the exhaust jet:

In the jet core area ($0 \le x \le x_{core}$):

$$\begin{cases} T = T_9 \\ F = F_9 \end{cases} \tag{22}$$

In the jet main area ($x \ge x_{core}$):

$$\begin{cases} \dfrac{T - T_0}{T_9 - T_0} = 1 - \exp\left[-1 / \left((0.25 - 0.04 M_9) \left(\dfrac{\rho_0}{\rho_9} \right)^{-0.22} \dfrac{x}{R_9} \left(\dfrac{\rho_0}{\rho_9} \right)^{0.5} - 2.3 \right) \right] \\ \dfrac{F}{F_9} = 1 - \exp\left[-1 / \left((0.25 - 0.04 M_9) \left(\dfrac{\rho_0}{\rho_9} \right)^{-0.22} \dfrac{x}{R_9} \left(\dfrac{\rho_0}{\rho_9} \right)^{0.5} - 2.3 \right) \right] \end{cases} \tag{23}$$

where, T is the local gas temperature; T_9 and T_0 represent the gas temperature at nozzle exit and ambient, respectively; x is the distance from the nozzle exit section; R_9 represents the radius of nozzle exit;

https://doi.org/10.1017/aer.2022.88 Published online by Cambridge University Press

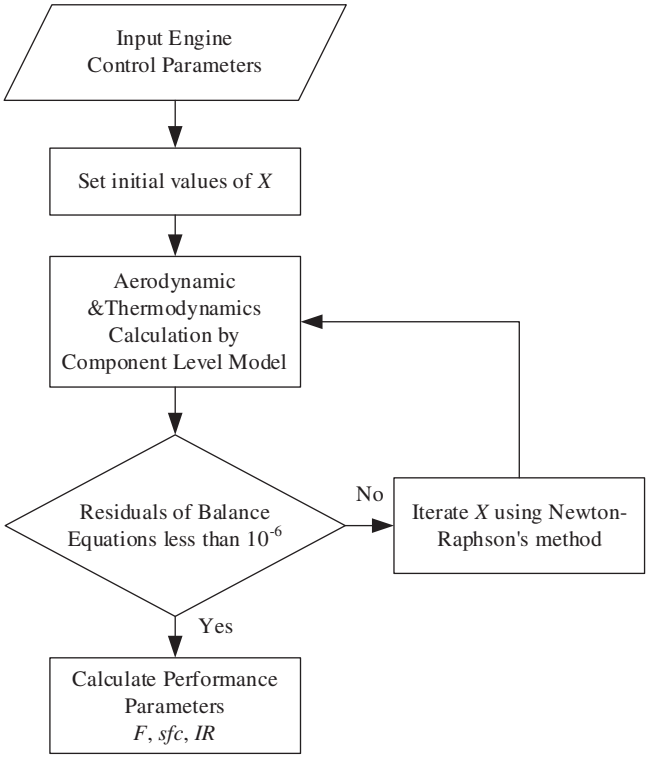

Figure 4. *Calculation flow of engine performance parameters.*

ρ represents the gas density; M_9 represents the Mach number of gas at the nozzle exit; x_{core} represents the length of the jet core area, and its calculation formula is:

$$x_{core} = \frac{9.2}{(1 - 0.16M_9)(\rho_0/\rho_9)^{0.28}} \cdot R_9 \tag{24}$$

The calculation flow of engine performance parameters is shown in Fig. 4.

3.0 Optimisation design methods and steps

The designed engine is equipped with an afterburner, so the ground state (on afterburner) was selected as the aerodynamic design point. For the fan, compressor and turbine, the scaling factor was determined by the design parameters of the aerodynamic design point and characteristic diagram (characteristic diagram similar to this component or general characteristic diagram), and then the component characteristics were determined. Besides the ground state, the subsonic cruise state and supersonic cruise state were typical working states. The technical limits of the engine were determined by the current technological limitations. Generally, the high- and low-pressure spool rotation speed, the metal temperature of turbine guide vanes and rotor blades, and the surge margin of fans and compressors are important technical limits. The thrust in each working state is the demand that must be met. Table 2 lists the performance requirements and design variable ranges of the engine under various operating conditions.

In this paper, the MOPSO algorithm was applied to the optimal design of a turbofan engine. At present, multi-objective optimisation methods are mainly divided into two categories: The first type is based on a single objective [22, 23], which combines multiple objectives into a single objective by applying some currently known correlations and then solving the single objective to obtain a single-point

https://doi.org/10.1017/aer.2022.88 Published online by Cambridge University Press

Table 2. *Performance requirements and design variable range under various operating conditions*

State		Ground	Subsonic cruise	Supersonic cruise
Thrust demand	F(kN)	150.0	25.0	49.2
Flight conditions	H(km)	0	8	10
	Ma	0	0.8	1.6
Design variable	Air intake W (kg/s)	120–135		
	Fan pressure ratio π_F	3–5		
	Compressor pressure ratio π_C	5–7		
	Burner exit total temperature T_{t4} (K)	<1,777	<1,777	<1,777
	Mixer entry Mach number M_6	0.3–0.6		
	Bypass ratio α	0.4–0.6		
	Cooling air fraction for the IFSGS ε_c	0	0.01–0.1	
	Cooling air fraction for the nozzle ε_w	0	0.01–0.1	
	The area ratio of the nozzle throat C_8	1	0.1–1	
	The area ratio of the nozzle exit C_9	1	0.1–1	

solution. Even with some standard methods such as the weighting method, constraint method and target programming method, the solution is dependent on the given weight of each target, and it is less likely to give a satisfactory solution to the problem. The second type, represented by the MOPSO algorithm, is based on a heuristic method, which realises the multi-directional and global search through a group-based search method, the optimisation result is a set of Pareto optimal solutions. The MOPSO algorithm was developed from the standard PSO algorithm [24]. The MOPSO algorithm can use efficient clustering to search the Pareto solutions in parallel, and multiple solutions can be generated in each iteration. The memory function of the algorithm makes the particles track the best solutions in the population and its own optimal solution at the same time, which makes the algorithm have high computational efficiency and execution speed. Aeroengine has a nonlinear mathematical model, and the aero-engine optimisation design problem has the characteristics of high nonlinearity, multi-objective, multi-constraints, and multi-design parameters, which makes the optimisation process easy to fall into local optimum. The MOPSO algorithm can effectively avoid falling into the local optimum because its particle count can be increased to ensure a large enough search range. The MOPSO algorithm does not depend on the functional characteristics of the problem and does not need to solve the gradient of the objective function, and it is more suitable to obtain the global optimal solution for complex functions. In the process of solving, even if some particles are abnormal, the whole algorithm will not collapse. In the MOPSO algorithm, each particle represents a potential solution. In a D-dimensional search space, each particle is regarded as a point in the space. Suppose the group is composed of m particles, and m is also called the group size. Let x_i be the D-dimensional position vector of the ith particle where $i = 1, 2, \ldots, m$; v_i is the flight speed of particle i; p_i is the optimal position of the individual, and p_g is the optimal group position. In each iteration, the particles update their speed and position according to the following formula:

$$v_i^{k+1} = wv_i^k + c_1 r_1 \left(p_i - x_i^k\right) + c_2 r_2 \left(p_g - x_i^k\right) \tag{25}$$

$$x_i^{k+1} = x_i^k + v_i^{k+1} \tag{26}$$

where k is the number of iterations, w is the inertia factor, r_1 and r_2 are random numbers between [0, 1], and c_1 and c_2 are the learning factor.

The main difference between the MOPSO algorithm and the standard PSO algorithm lies in selecting the individual optimal p_i and the group optimal p_g. In each iteration, the p_i and p_g of the standard PSO algorithm are uniquely determined. In contrast, the MOPSO algorithm obtains the Pareto solution set,

https://doi.org/10.1017/aer.2022.88 Published online by Cambridge University Press

and there are multiple non-inferior solutions, so it is necessary to select p_i and p_g individual for each particle separately, and the method is as follows:

1. Select individual optimal p_i based on the Pareto dominance method: Select non-dominated particles as the individual optimal value from the current particle position and the individual's historical optimal position. If none of them can dominate the pair, one is randomly selected.
2. Select the optimal group p_g based on the roulette method: First, a set of non-inferior solutions needs to be established. Each particle will select one of the non-inferior solutions as its optimal value p_g of the group. The probability that the non-inferior solution in the set is selected is based on its aggregation radius. The aggregation radius refers to the average distance of the non-inferior solution from the left and right neighbouring particles in the target space. The fewer other particles around the non-inferior solution particles, the higher the probability of being selected. According to the size of the aggregation radius of each non-inferior solution, a roulette method is used to select the global optimal value p_g from the non-inferior solution set for each particle.

Compared with the standard PSO algorithm, the MOPSO algorithm usually requires a larger population size, and more computing resources will be consumed. To shorten the calculation time and improve the efficiency of CPU utilisation, a multi-threaded parallel MOPSO optimisation program was developed in this paper. The implementation steps were as follows:

Step 1. Determine the threshold of the design variables to be optimised (Table 2).

Step 2. Establish an orthogonal array based on the range of the design variables. Use the orthogonal table to initialise the position of the particle swarm. Each particle represented a set of design variables. The initial velocity of the particle swarm was 0.

Step 3. When the main thread was blocked, start the multi-threads to calculate fitness (objective function values) corresponding to each particle in parallel, and check whether all constraints were met (e.g., high-pressure spool rotation speed $n_H < 100\%$, low-pressure spool rotation speed $n_L < 100\%$, fan surge margin $SM_F < 0.25$, compressor surge margin $SM_C < 0.25$, and the minimum thrust constraint in Table 2). If not, the particle fitness would be given an infinite value.

Step 4. Close the multi-threads, and update the Pareto solution set, delete inferior solutions, and add new non-inferior solutions in the main thread.

Step 5. Calculate the distance between non-inferior solutions in the target space and the aggregation radius of each solution.

Step 6. For each particle, select the individual optimal p_i based on the Pareto dominance method and select the group optimal p_g based on the roulette method.

Step 7. The inertia factor w was set to 0.4, and the learning factors c_1 and c_2 were set to 2. Update the velocity v_i of each particle according to Equation (25), update the position x_i of each particle according to Equation (26), and reset the position of particles beyond the search space.

Step 8. If the maximum number of iterations was reached, stop searching and output the search results. Otherwise, return to step 3 to continue searching.

4.0 Optimisation results

In this paper, a turbofan engine with a small bypass ratio without infrared stealth capability was used as the reference engine (column I in Table 7). The air intake W_{TO} (subscript *TO* indicates ground state) in the ground state was 135kg/s; the fan pressure ratio $\pi_{F,TO}$ was 5, the compressor pressure ratio $\pi_{C,TO}$ was 7; the burner exit total temperature $T_{t4,TO}$ was 1,777K; the mixer entry Mach number $M_{6,TO}$ was 0.4; the bypass ratio α_{TO} was 0.4; the burner exit total temperature $T_{t4,CR1}$ (subscript *CR*1 indicates subsonic cruise state) in the subsonic cruise state was 1,310K; the burner exit total temperature $T_{t4,CR2}$ (subscript

https://doi.org/10.1017/aer.2022.88 Published online by Cambridge University Press

$CR2$ indicates supersonic cruise state) in the supersonic cruise was 1,590K. The ground state thrust F_{TO} of the reference engine was 177kN; the specific fuel consumption rate sfc_{CR1} in the subsonic cruise state was 22.10mg/N/s; the infrared radiation intensity IR_{CR1} in subsonic cruise state was 706W/sr; the specific fuel consumption rate sfc_{CR2} in supersonic cruise state was 27.87mg/N/s; the infrared radiation intensity IR_{CR2} in supersonic cruise state was 2223W/sr.

4.1 The reference engine refitted with infrared radiation suppression module

The design parameters of the reference engine at the aerodynamic design point had been determined, so there were five design variables to be optimised in the cruise state, namely, the total temperature $T_{t4,CR}$ at the burner exit, the cooling air fraction $\varepsilon_{c,CR}$ for the IFSGS, the cooling air fraction $\varepsilon_{w,CR}$ for the nozzle expansion section, the area ratio $C_{8,CR}$ of the nozzle throat and the area ratio $C_{9,CR}$ of the nozzle exit. Nozzle throat area $A_{8,CR}$, and exit area $A_{9,CR}$ could be adjusted. The calculation formula of nozzle throat area $A_{8,CR}$ in cruise state is:

$$A_{8,CR} = A_{8,TO} \cdot C_{8,CR} \tag{27}$$

where, $A_{8,TO}$ is the nozzle throat area in the ground state, which is determined by the ground state design parameters. The calculation formula of nozzle exit area $A_{9,CR}$ in cruise state is:

$$A_{9,CR} = A_{8,CR} + C_{9,CR} \cdot (A_{9ideal,CR} - A_{8,CR}) \tag{28}$$

where, $A_{9ideal,CR}$ is the ideal nozzle exit area in the cruise state, which means the gas expands completely in the nozzle, and the static pressure at the nozzle exit is equal to atmospheric pressure. The nozzle throat area $A_{8,CR}$, and nozzle exit area $A_{9,CR}$ determine the backward visible area of high-temperature components such as IFSGS and nozzle expansion section, which has an important impact on the infrared radiation intensity of the exhaust system.

The change in engine performance with a single design variable is shown in Fig. 5. It can be seen that increasing the cooling airflow fraction or shrinking the area of the nozzle throat and exit can inhibit the infrared radiation intensity of the engine. Among them, increasing the cooling airflow ratio $\varepsilon_{c,CR}$ of the IFSGS has the best infrared suppression effect, while shrinking the area of nozzle outlet $A_{9,CR}$ not only reduces the infrared radiation intensity but also leads to a significant decrease in thrust and a significant increase in fuel consumption. In addition, reducing the total temperature $T_{t4,CR}$ at the burner exit plays a positive role in both reducing the intensity of infrared radiation and the specific fuel consumption rate. It can be noticed that when $\varepsilon_{c,CR}$ and $\varepsilon_{w,CR}$ are equal, the sfc_{CR} in Fig. 5(a) is smaller than that in Fig. 5(b). The cooling air for the IFSGS is introduced from the bypass duct, which is equivalent to mixing part of the bypass flow with the core flow before the mixer, and the impact on the engine performance only comes from the flow loss in the air entrainment pipeline, while the cooling air for the nozzle expansion section is not rectified and accelerated in the contraction section of the nozzle, and most of its kinetic energy will be lost after mixing with the gas in the expansion section of the nozzle.

Taking the specific fuel consumption rate sfc_{CR} and infrared radiation intensity IR_{CR} as the optimisation objectives, the performance optimisation solutions at the subsonic and supersonic cruise state of the reference engine refitted with infrared suppression module were obtained respectively, as shown in the Figs 6 and 7. When the specific fuel consumption rate sfc_{CR1} of the engine refitted with infrared suppression module was equal to that of the reference engine without infrared stealth capability, the infrared radiation intensity IR_{CR1} of the refitted engine decreased by 39.0% (column II in Table 7). Under the condition of meeting the minimum thrust requirements in the subsonic cruise state, the maximum reduction of infrared radiation intensity IR_{CR1} could reach 47.7% (column III in Table 7).

When the specific fuel consumption rate sfc_{CR2} of the engine refitted with infrared suppression module was equal to that of the reference engine without infrared stealth capability, the infrared radiation intensity IR_{CR2} of the refitted engine decreased by 30.8% (column IV in Table 7). Under the condition of meeting the minimum thrust requirements in the supersonic cruise state, the maximum reduction of infrared radiation intensity IR_{CR2} could reach 39.9% (column V in Table 7).

https://doi.org/10.1017/aer.2022.88 Published online by Cambridge University Press

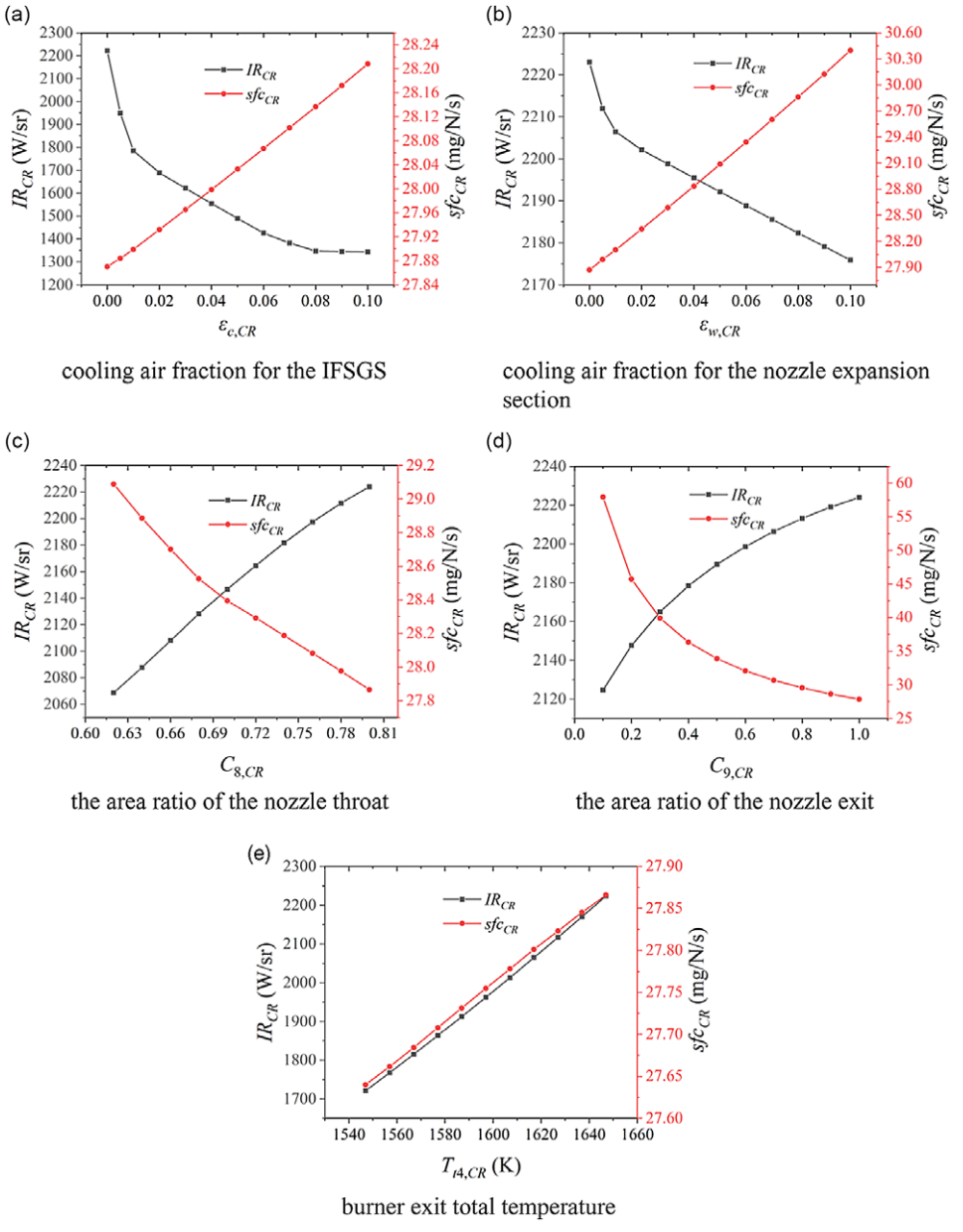

Figure 5. *The change of engine performance parameters with a single design variable.*

In the solution set, the nozzle throat area ratio $C_{8,CR}$ has a strong positive correlation with the infrared radiation intensity IR_{CR}, while there is a strong negative correlation between the cooling air fraction $\varepsilon_{c,CR}$ for the IFSGS and IR_{CR}. The nozzle exit area ratio $C_{9,CR}$ is close to the upper limit value of 1, and the cooling air fraction $\varepsilon_{w,CR}$ for the nozzle expansion section is close to the lower limit value of 0.01. In the solution set with lower infrared radiation intensity IR_{CR}, the burner exit total temperature $T_{t4,CR}$ is slightly higher than that with higher infrared radiation intensity. In general, the reference engine refitted with an infrared suppression module can reduce the infrared radiation intensity by shrinking the nozzle throat area ratio and increasing the cooling air fraction for the IFSGS, while shrinking the nozzle exit area or increasing the cooling air fraction for the nozzle expansion section is not the best choice.

https://doi.org/10.1017/aer.2022.88 Published online by Cambridge University Press

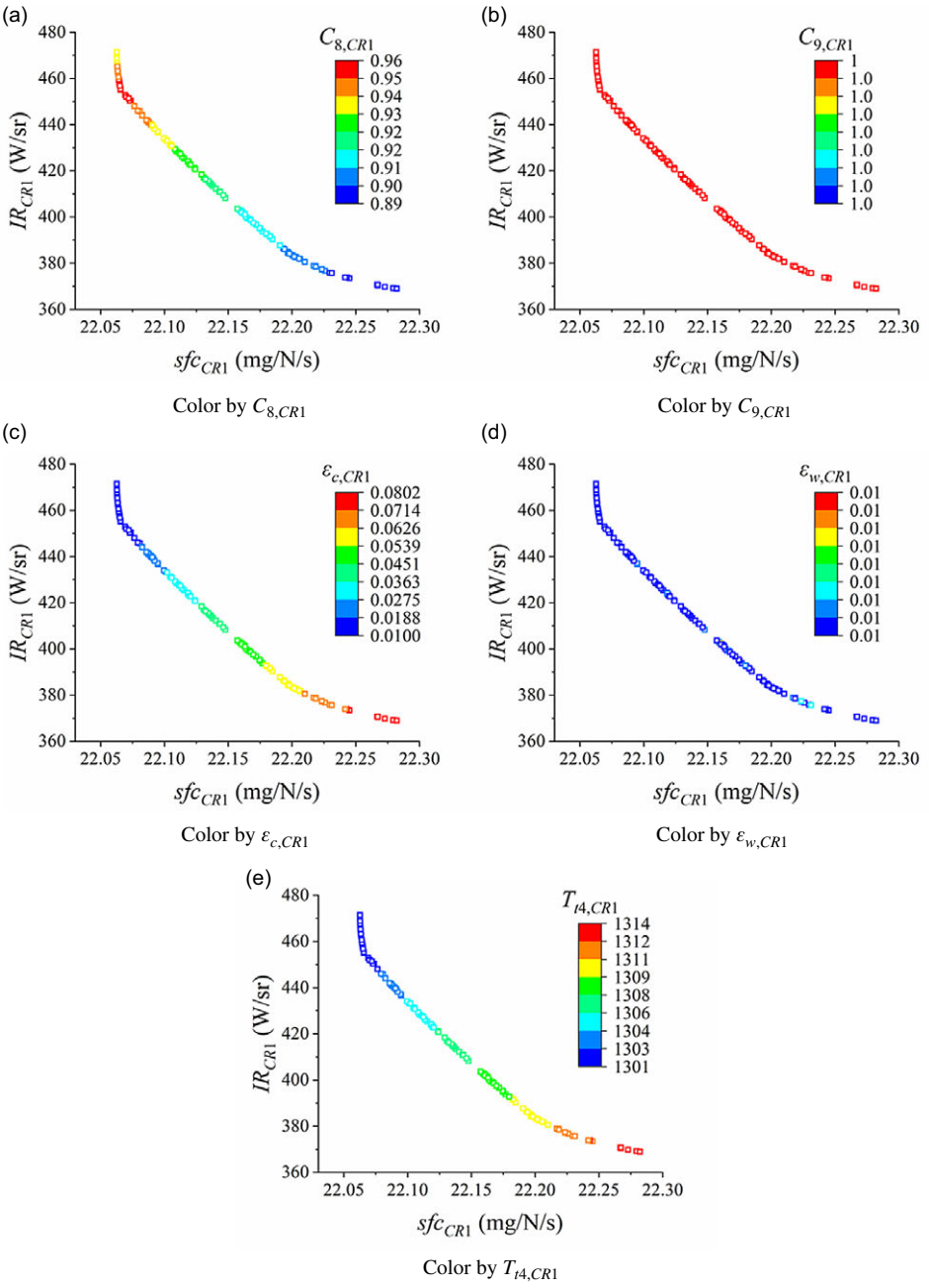

Figure 6. *Performance optimisation of the reference engine refitted with infrared suppression module in subsonic cruise state.*

4.2 Cycle optimisation design through MDPs concept

The engine refitted with the infrared suppression module described above had certain cycle parameters, which limited the infrared stealth performance of the engine. To obtain a more ideal infrared stealth effect, the cycle optimisation design of the turbofan engine was carried out. In the cycle optimisation design using the MOPSO method, both the ground state and cruise state were set as the engine design points through the MDPs concept. The cycle parameters of the ground state and the adjustable

https://doi.org/10.1017/aer.2022.88 Published online by Cambridge University Press

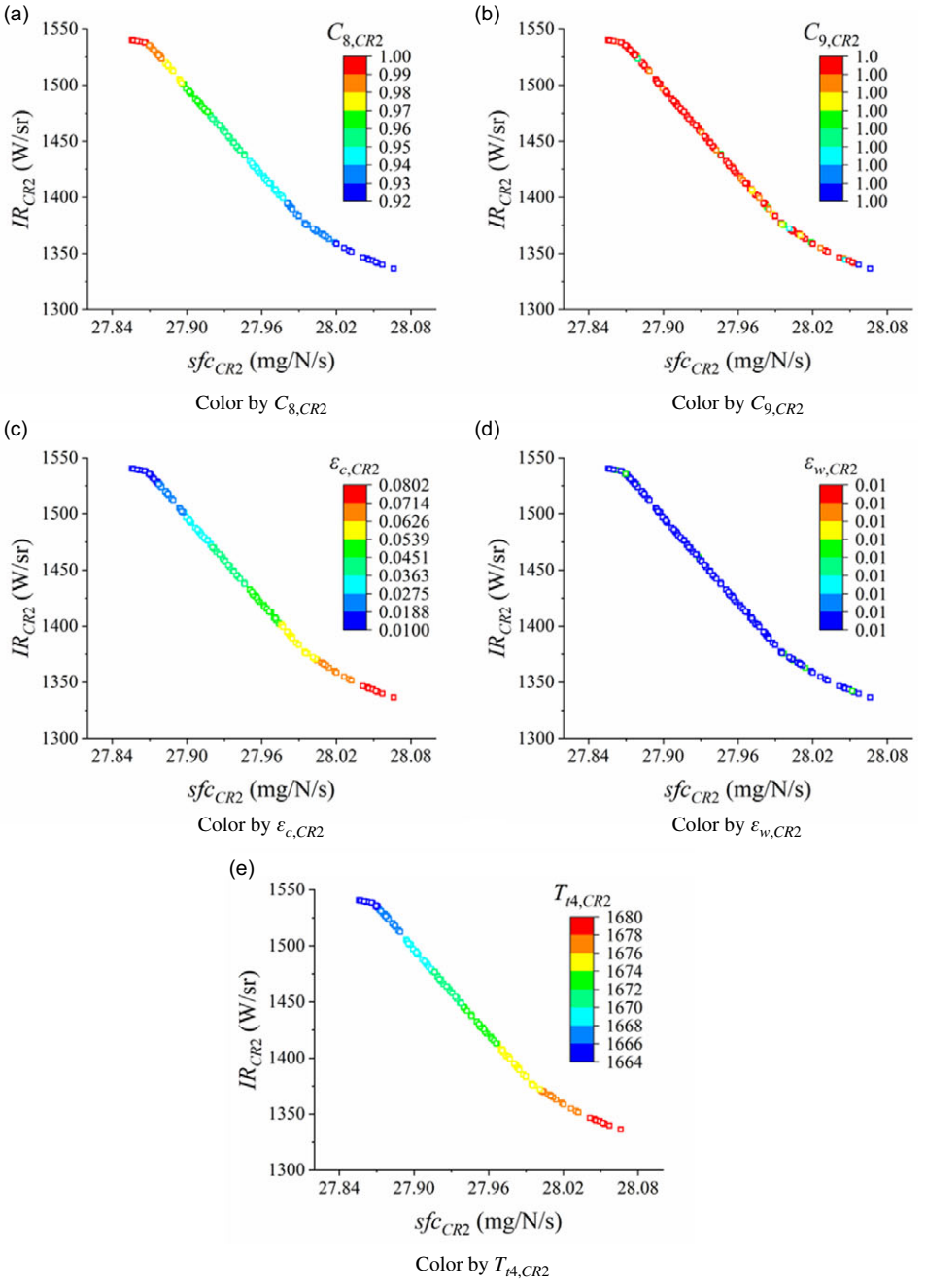

Figure 7. *Performance optimisation of the reference engine refitted with infrared suppression module in supersonic cruise state.*

parameters of the cruise state could be mixed into a set of optimisation variables, and the performance parameters of the two states could also be mixed into a set of optimisation targets. The performance constraints of each design point in Table 2 must be ensured to be met. Two sets of optimisation design schemes were given in this paper. Scheme 1 took the specific fuel consumption rate sfc_{CR1}, backward

https://doi.org/10.1017/aer.2022.88 Published online by Cambridge University Press

Table 3. *Performance parameter intervals corresponding to design domains of scheme 1*

Design domains	A1	B1	C1	D1
F_{TO} (kN)	176–180	150–172	150–176	150–176
IR_{CR1} (W/sr)	166–445	166–445	126–166	166–445
sfc_{CR1} (mg/N/s)	21.77–22.74	21.45–21.61	21.77–22.58	21.61–22.25

Table 4. *Performance parameter intervals corresponding to design domains of scheme 2*

Design domains	A2	B2	C2	D2
F_{TO} (kN)	176–180	150–172	150–176	150–176
IR_{CR2} (W/sr)	764–1,492	764–1,492	660–764	764–1,492
sfc_{CR2} (mg/N/s)	27.61–28.67	27.26–27.44	27.44–28.14	27.44–27.97

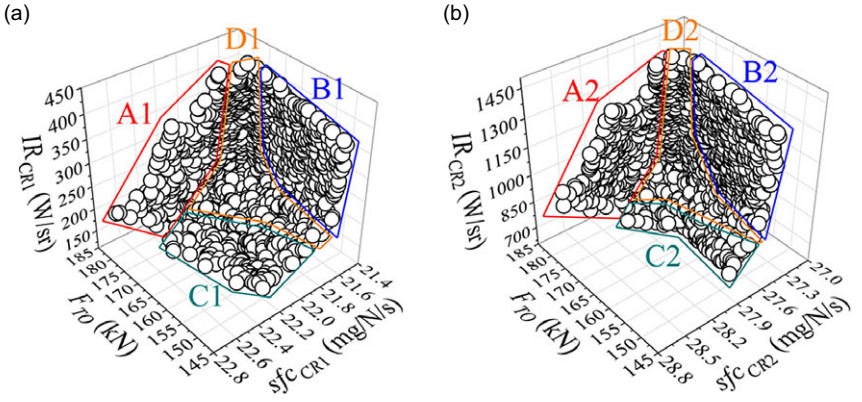

Scheme 1 design domain partition Scheme 2 design domain partition

Figure 8. *Design domain partition.*

infrared radiation intensity IR_{CR1} in subsonic cruise state and thrust F_{TO} in ground state as the optimisation objectives, and scheme 2 took the specific fuel consumption rate sfc_{CR2}, backward infrared radiation intensity IR_{CR2} in supersonic cruise state and thrust F_{TO} in ground state as the optimisation objectives. The design variables to be optimised include the air intake W_{TO}, fan pressure ratio $\pi_{F,TO}$, compressor pressure ratio $\pi_{C,TO}$, burner exit total temperature $T_{t4,TO}$ and $T_{t4,CR}$, mixer entry Mach number $M_{6,TO}$, bypass ratio α_{TO}, the cooling air fraction $\varepsilon_{c,CR}$ for the IFSGS, the cooling air fraction $\varepsilon_{w,CR}$ for the nozzle expansion section, area ratio $C_{8,CR}$ of the nozzle throat and area ratio $C_{9,CR}$ of the nozzle exit.

Figure 8 shows the design domain optimised by schemes 1 and 2. In the three-dimensional target space, the optimised Pareto solution set constitutes an irregular surface. Pareto solution sets can be divided into four design domains: ground state high thrust design domain A, cruise state low fuel consumption design domain B, cruise state low infrared characteristic design domain C and performance balance design domain D. The performance parameters corresponding to the design domains are shown in Tables 3 and 4.

According to scheme 1 in Fig. 8(a), when F_{TO} and sfc_{CR1} of cycle optimised design engine is equal to that of the reference engine without infrared stealth capability, IR_{CR1} of the cycle optimised design engine decreases by 67.9% (column VI in Table 7), and the maximum reduction of IR_{CR1} can reach 82.2% (column VII in Table 7) when meeting the minimum thrust requirements in the subsonic cruise state.

According to scheme 2 in Fig. 8(b), when F_{TO} and sfc_{CR2} of cycle optimised design engine is equal to that of the reference engine without infrared stealth capability, IR_{CR2} of the cycle optimised design

https://doi.org/10.1017/aer.2022.88 Published online by Cambridge University Press

Table 5. *Design variables corresponding to design domains of scheme 1*

Design domains	A1	B1	C1	D1
W_{TO} (kg/s)	135	135	133–135	135
$\pi_{F,TO}$	4.9–5	3.8–4.6	3.8–4.7	4.1–5
$\pi_{C,TO}$	7	7	7	7
$T_{t4,TO}$ (K)	1,708–1,777	1,535–1,742	1,500–1,673	1,535–1,777
$M_{6,TO}$	0.4–0.54	0.4–0.42	0.4–0.47	0.4–0.44
α_{TO}	0.3–0.49	0.56–0.6	0.3–0.41	0.37–0.6
$T_{t4,CR1}$ (K)	1,212–1,301	1,212–1,301	1,145–1,212	1,190–1,324
$C_{8,CR1}$	0.85–0.97	0.74–0.82	0.74–0.88	0.77–0.88
$C_{9,CR1}$	0.96–1	1	0.98–1	1
$\varepsilon_{c,CR1}$	0.01–0.1	0.01–0.1	0.077–0.1	0.01–0.1
$\varepsilon_{w,CR1}$	0.01–0.022	0.01–0.026	0.01	0.01

Table 6. *Design variables corresponding to design domains of scheme 2*

Design domains	A2	B2	C2	D2
W_{TO} (kg/s)	135	135	135	135
$\pi_{F,TO}$	4.9–5.0	4–4.6	4.1–4.9	4.2–5
$\pi_{C,TO}$	7	7	7	7
$T_{t4,TO}$ (K)	1,708–1,777	1,569–1,742	1,500–1,673	1,569–1,777
$M_{6,TO}$	0.4–0.54	0.4–0.42	0.4–0.47	0.43–0.54
α_{TO}	0.3–0.49	0.52–0.60	0.3–0.41	0.37–0.6
$T_{t4,CR2}$ (K)	1,570–1,649	1,543–1,649	1,464–1,543	1,517–1,675
$C_{8,CR2}$	0.88–1	0.76–0.85	0.76–0.91	0.79–0.91
$C_{9,CR2}$	0.94–1	0.99–1	0.97–1	0.99–1
$\varepsilon_{c,CR2}$	0.01–0.1	0.01–0.1	0.066–0.1	0.01–0.1
$\varepsilon_{w,CR2}$	0.01–0.012	0.01	0.01–0.011	0.01

engine decreases by 52.1% (column VIII in Table 7), and the maximum reduction of IR_{CR2} can reach 70.3% (column IX in Table 7) when meeting the minimum thrust requirements in the supersonic cruise state. Therefore, the infrared stealth performance of the cycle optimised engine was better than that of the reference engine refitted with infrared suppression module.

Figures 9 and 10 respectively show the performance optimal solution and corresponding design variables after the cycle optimisation design of schemes 1 and 2. Tables 5 and 6 lists the design variable intervals corresponding to the design domains of schemes 1 and 2 respectively.

The optimised ground state air intake W_{TO} is close to the upper limit, and a larger air intake means a larger engine size and larger infrared radiation area. However, for two engines with similar geometry, the one with a larger size can work at lower throttle under the set thrust demand. Therefore, in general, the design of a larger air intake is conducive to reducing the infrared radiation characteristics of the engine.

In the solution sets, the bypass ratio α_{TO} has a strong negative correlation with specific fuel consumption rate sfc_{CR} and a strong positive correlation with infrared radiation intensity IR_{CR}. Because the surface temperature of the components in the core stream duct is much higher than that in the bypass duct, the strong infrared radiation surface area of the engine with a smaller bypass ratio is also smaller when the total air intake is the same. Another clear trend is: In the low infrared characteristic design domain, when the corresponding burner exit total temperature in the ground state and cruise state are both close to the lower limit, the cooling air fraction for the IFSGS is close to the upper limit of 0.1.

Similar to the results in Figs 6 and 7, $C9_{,CR}$ is close to the upper limit value of 1 in most design domains, $\varepsilon_{w,CR}$ is close to the lower limit of 0.01. This shows that it is not the best choice to reduce the

https://doi.org/10.1017/aer.2022.88 Published online by Cambridge University Press

Table 7. *Comparison of optimisation design results*

	No.	I	II	III	IV	V	VI	VII	VIII	IX
Performance parameters	F_{TO} (kN)	177	177	177	177	177	177	151	177	150
	sfc_{CR1} (mg/N/s)	22.10	22.10	22.28			22.10	22.18		
	IR_{CR1} (W/sr)	706	431	369			227	126		
	sfc_{CR2} (mg/N/s)	27.87			27.87	28.07			27.87	27.78
	IR_{CR2} (W/sr)	2,223			1,538	1,336			1,065	661
Design variables	W_{TO} (kg/s)	135	135	135	135	135	135	135	135	135
	$\pi_{F,TO}$	5	5	5	5	5	5	3.9	5	4.3
	$\pi_{C,TO}$	7	7	7	7	7	7	7	7	7
	$T_{t4,TO}$ (K)	1,777	1,777	1,777	1,777	1,777	1,777	1,500	1,777	1,500
	$M_{6,TO}$	0.4	0.4	0.4	0.4	0.4	0.46	0.46	0.47	0.43
	α_{TO}	0.4	0.4	0.4	0.4	0.4	0.41	0.3	0.405	0.3
	$T_{t4,CR1}$ (K)	1,293	1,305	1,314			1,282	1,145		
	$C_{8,CR1}$	0.8	0.93	0.89			0.91	0.88		
	$C_{9,CR1}$	1	1	1			1	1		
	$\varepsilon_{c,CR1}$	0	0.029	0.080			0.067	0.089		
	$\varepsilon_{w,CR1}$	0	0.01	0.01			0.01	0.01		
	$T_{t4,CR2}$ (K)	1,647			1,665	1,680			1,636	1,469
	$C_{8,CR2}$	0.8			0.99	0.92			0.9	0.83
	$C_{9,CR2}$	1			1	1			1	1
	$\varepsilon_{c,CR2}$	0			0.013	0.080			0.036	0.1
	$\varepsilon_{w,CR2}$	0			0.01	0.01			0.01	0.01

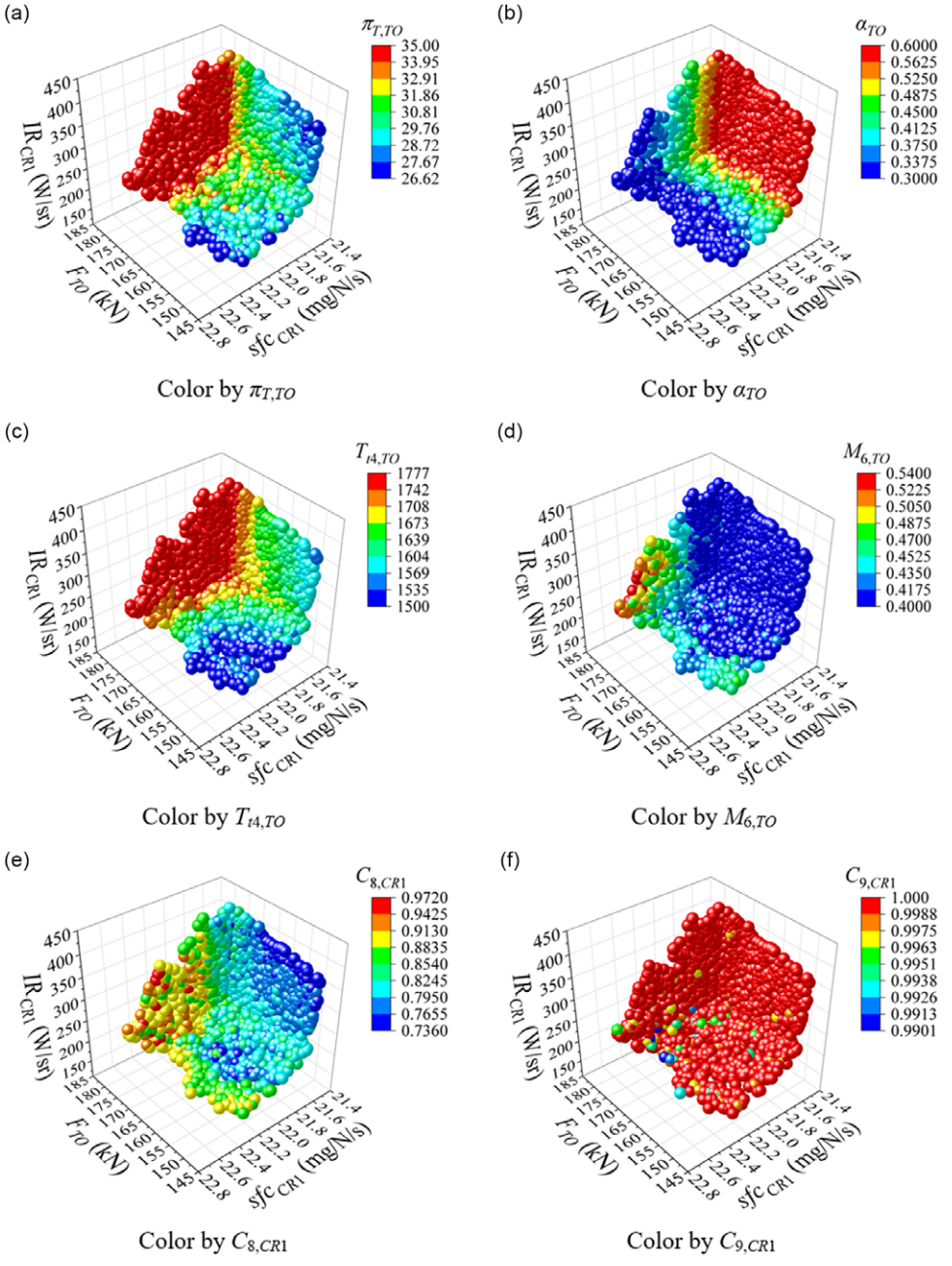

Figure 9. *Optimal performance solution and corresponding design variables of scheme 1.*

infrared radiation characteristics for an engine with cycle optimisation design by shrinking the exit area of the nozzle or increasing the cooling air fraction for the expansion section of the nozzle.

5.0 Uncertainties analysis of engine design

The uncertainty of aero-engine performance comes from two aspects: First, the influence of objective factors such as manufacturing technology and assembly technology; then, due to the factors of wear,

https://doi.org/10.1017/aer.2022.88 Published online by Cambridge University Press

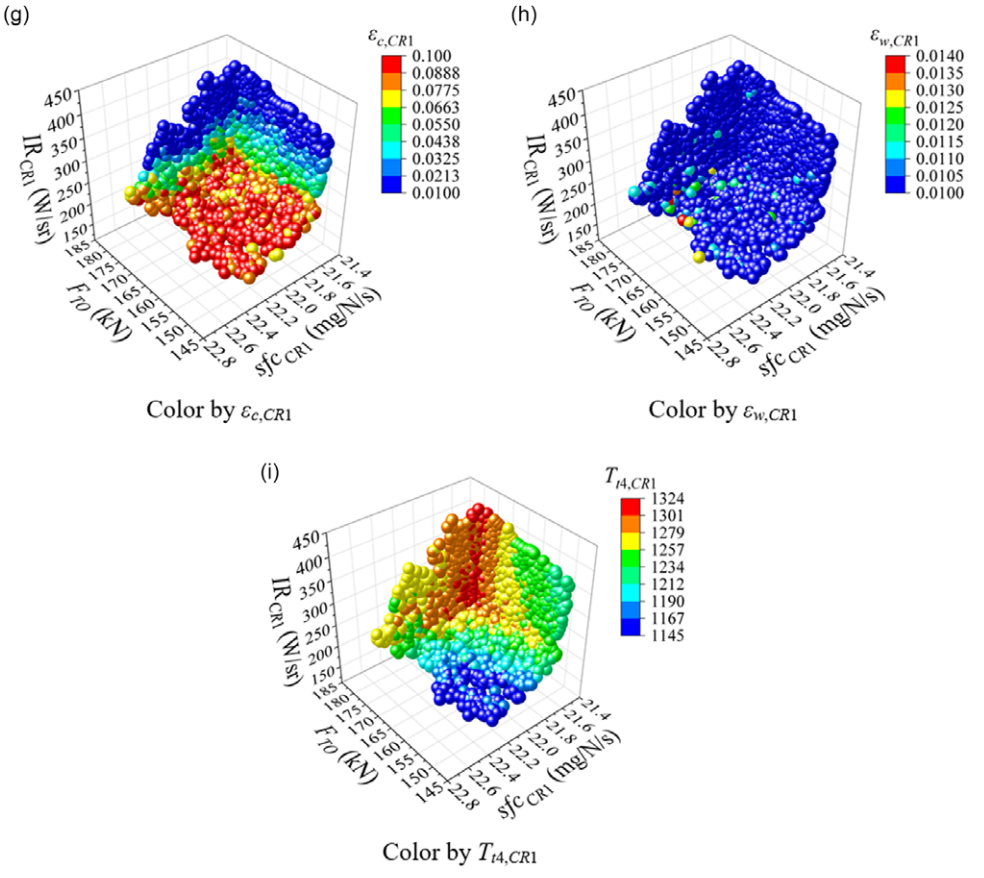

Figure 9. *Continued.*

blade fouling and foreign objects' injury after service, the performance of each component changes indeterminacy. The compressor, turbine and other rotating parts are the core parts of the engine, the uncertainty of the characteristics of rotating parts was studied in this paper. In the overall design stage of the engine, the detailed geometric dimensions of the rotating parts are undetermined, so the usual method is to set the deviation factor to simulate the uncertainty of the parts' characteristics. The following deviation factors were considered in this paper:

$$D_{\eta,F}=1-\frac{\eta_F}{\eta_{F,i}},\quad D_{\eta,C}=1-\frac{\eta_C}{\eta_{C,i}},\quad D_{\eta,H}=1-\frac{\eta_H}{\eta_{H,i}},\quad D_{\eta,L}=1-\frac{\eta_L}{\eta_{L,i}},$$
$$D_{w,F}=1-\frac{w_F}{w_{F,i}},\quad D_{w,C}=1-\frac{w_C}{w_{C,i}},\quad D_{w,H}=1-\frac{w_H}{w_{H,i}},\quad D_{w,L}=1-\frac{w_L}{w_{L,i}},$$

where D_η represents the deviation factor of efficiency; D_w represents the deviation factor of flow rate; η represents the efficiency; w represents the flow rate; and the subscript F represents the fan, C represents the compressor, H represents the HP turbine, L represents the LP turbine, i represents the design value.

Sensitivity analysis was used to evaluate the influence of uncertain factors on engine performance. Sensitivity is defined as the ratio of the percentage change of engine performance parameter to the deviation factor, for example, the sensitivity S of thrust to compressor efficiency deviation factor:

$$S(F)=\frac{\Delta F/F}{D_{\eta,C}} \tag{29}$$

https://doi.org/10.1017/aer.2022.88 Published online by Cambridge University Press

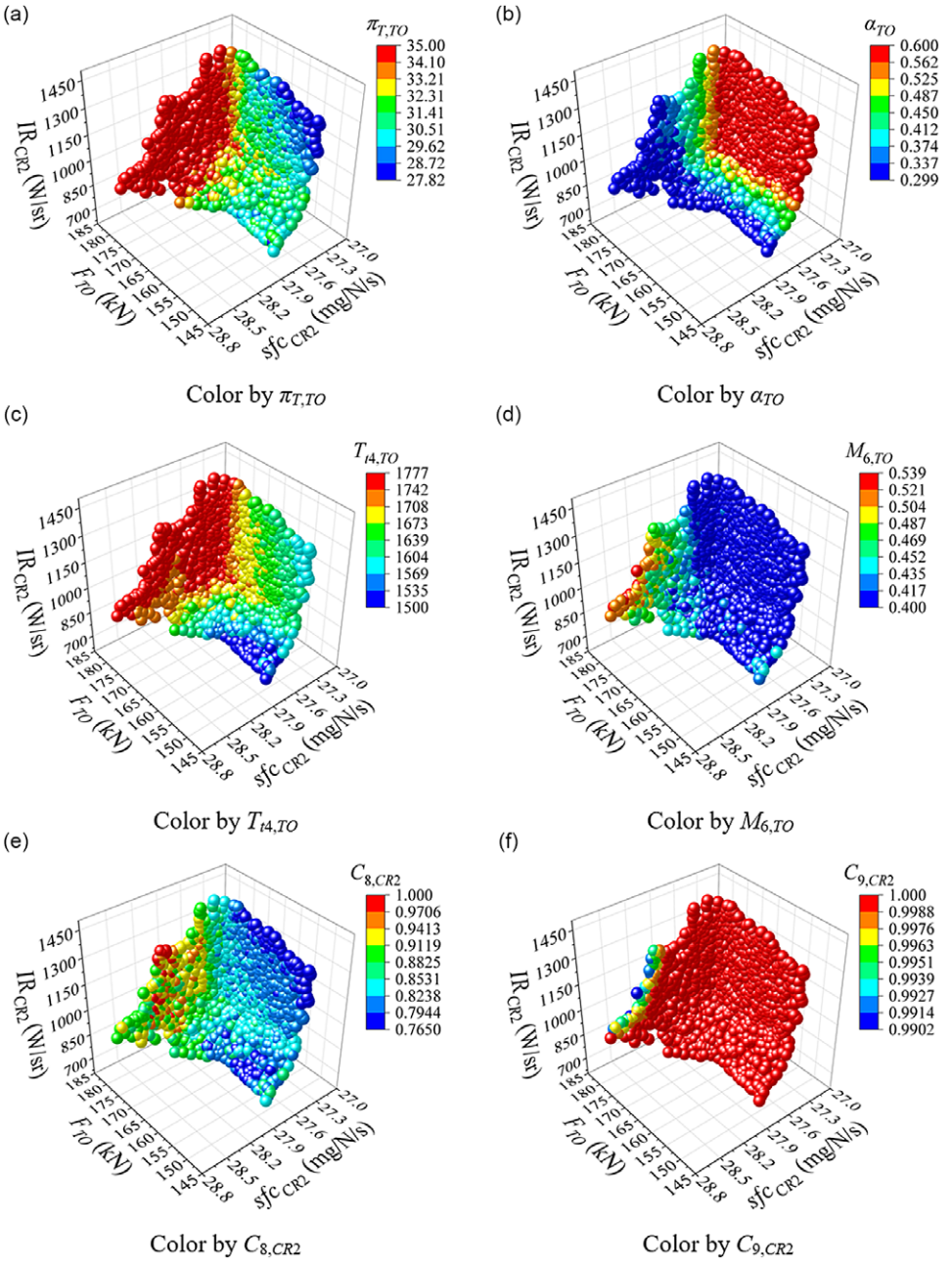

Figure 10. *Optimal performance solution and corresponding design variables of scheme 2.*

Table 8 shows the results of sensitivity analysis when the deviation factor was set to 1%. When the efficiency and flow rate of the fan and compressor is lower than the set values, the thrust of the engine is also lower than the design values, and the specific fuel consumption rate and infrared radiation intensity are higher than the design values. When the flow rate of the turbines is slightly lower than the design value, the thrust of the engine is increased, but the opposite is true for the fan and compressor.

The influence of a single uncertain factor on engine performance is analysed above. Next, the distribution of engine performance parameters was tested when the eight uncertain factors were coupled.

https://doi.org/10.1017/aer.2022.88 Published online by Cambridge University Press

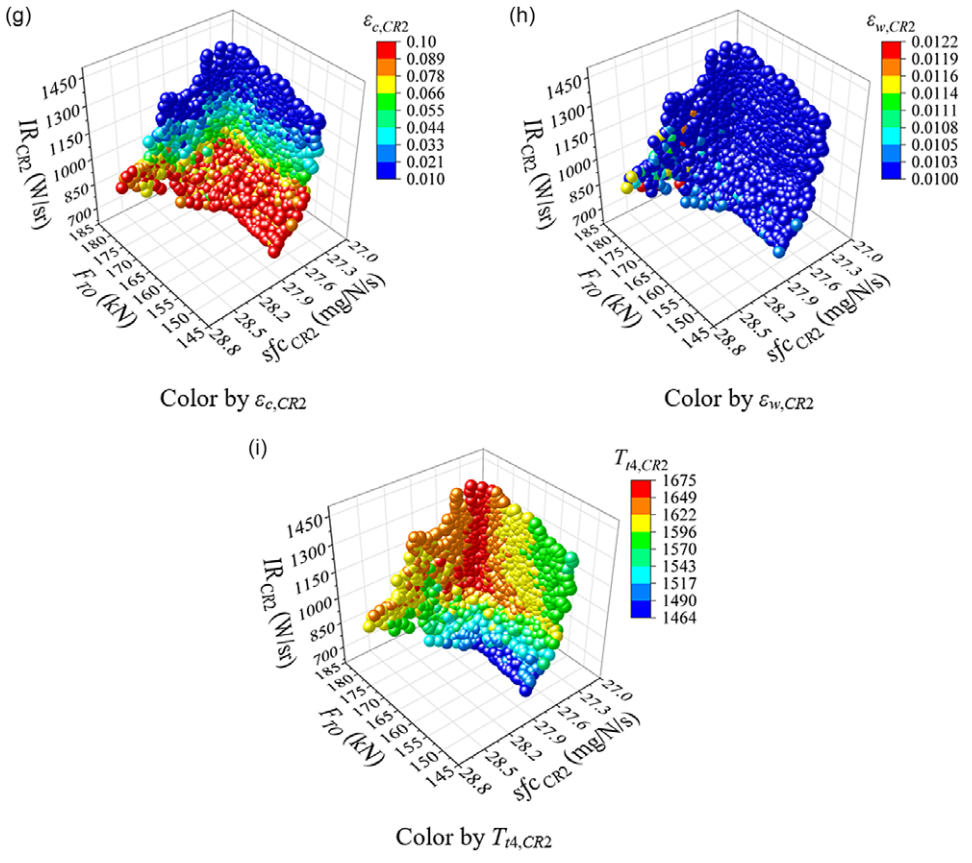

Figure 10. *Continued.*

Assuming that the deviation factors are distributed normally, the average deviation $\mu = 0$, and the standard deviation σ satisfies $3\sigma = 1\%$. That is, 99.74% of the deviation factor falls between regions (μ-3σ, μ+3σ). 3,000 groups of samples with random deviation factors were tested, and the distribution of engine performance parameters is shown in Fig. 11. It can be seen that the engine performance parameters also conform to the normal distribution. The standard deviation of thrust and fuel consumption is about 0.2%, and that of infrared is about 1.3%. Therefore, it is reasonable to set some margin when determining the engine performance index, which will ensure that most of the actually manufactured engines achieve the expected performance. From the above analysis, a thrust margin of 0.6% is recommended to set.

6.0 Conclusions

In this paper, the performance of a turbofan engine using infrared stealth technologies was optimised based on the MOPSO algorithm. The main conclusions are as follows:

(1) In the cruising state, the backward infrared characteristics of turbofan engines could be effectively reduced by using the IFSGS with air film cooling technologies, which causes low thrust loss and a slight increase in fuel consumption rate. However, reducing the nozzle exit area or increasing the cooling air fraction for the nozzle expansion section would not only reduce the infrared characteristics but also greatly increase the fuel consumption, so it is not the best solution.

https://doi.org/10.1017/aer.2022.88 Published online by Cambridge University Press

Table 8. *Sensitivity analysis*

Deviation factors	$S(F)$	$S(sfc)$	$S(IR)$
$D_{\eta,F}$	–0.33708	+0.33822	+1.22824
$D_{\eta,C}$	–0.19527	+0.19565	+1.9509
$D_{\eta,H}$	–0.24481	+0.24541	+2.45093
$D_{\eta,L}$	–0.32424	+0.32529	+1.31431
$D_{w,F}$	–0.08887	+0.08895	+0.31877
$D_{w,C}$	–0.10321	+0.10332	+1.02724
$D_{w,H}$	+0.03399	–0.03398	–0.33639
$D_{w,L}$	+0.08498	–0.08491	+0.58007

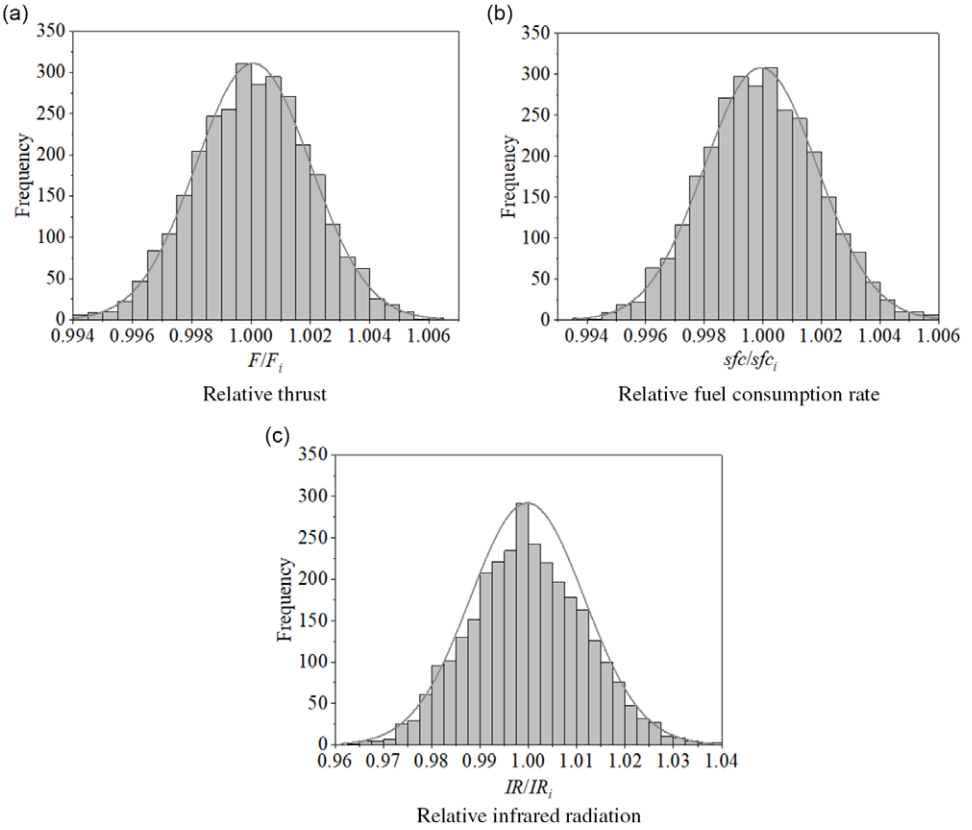

Figure 11. *Performance histogram of No. IX engine.*

(2) The performance of the reference engine refitted with an infrared suppression module in cruise state was optimised. In subsonic and supersonic cruise states, when the specific fuel consumption rate of the engine refitted with infrared suppression module was equal to that of the reference engine without infrared stealth capability, the infrared radiation intensity of the refitted engine decreased by 39.0% and 30.8%, separately, and under the condition of meeting the minimum thrust requirements in cruise state, the maximum reduction of infrared radiation intensity could reach 47.7% and 39.9%, separately.

(3) Based on the concept of MDPs, the cycle optimisation design of the turbofan engine was carried out with the optimisation objectives of the specific fuel consumption rate, infrared radiation intensity in the cruise state, and thrust in the ground state. In subsonic and supersonic cruise

https://doi.org/10.1017/aer.2022.88 Published online by Cambridge University Press

states, when the thrust and the specific fuel consumption rate of cycle optimised design engine were equal to that of the reference engine without infrared stealth capability, the infrared radiation intensity of the cycle optimised design engine decreases by 67.9% and 52.1%, separately, and when meeting the minimum thrust requirements in cruise state, the maximum reduction of infrared radiation intensity can reach 82.2% and 70.3%, separately.

Acknowledgements. This study is supported by National Science and Technology Major Project under Grant J2019-III-0009-0053.

Conflicts of interest. The author(s) declare none.

References

[1] Morris, T., Marciniak, M., Wollenweber, G. and Turk, J. Analysis of uncertainties in infrared camera measurements of a turbofan engine in an altitude test cell, *Infrared Phys. Technol.*, 2006, **48**, (2), pp 130–153.
[2] Deng, H., Shang, S., Jin, H., Yang, S. and Wang, X. Analysis and discussion on stealth technology of aero engine, *Aeronaut. Sci. Technol.*, 2017, **28**, (10), pp 1–7.
[3] Zhang, W. *Research on Controlling of Infrared Radiant with Cooling of Components at Aeroengine Exhaust System*, Xihua University, Chengdu, China, 2011.
[4] Gong, Y. *Design and Performance Simulation of an Experimental Rig for Infrared stealth research of Exhaust System of a Turbofan Engine*, Nanjing University of Aeronautics and Astronautics, Nanjing, China, 2007.
[5] Wang, D. and Ji, H. Model experiment and numerical analysis on infrared character of lobed mixer exhaust system, *Infrared Laser Eng.*, 2017, **46**, (1), pp 1–7.
[6] Wang, H. *Investigation on Several Issues in Low Infrared Signature Turbofan Engine Design*, Nanjing University of Aeronautics and Astronautics, Nanjing, China, 2020.
[7] Wang, H., Ji, H., Sang, X. and Wang, Y. Effects of fully shielded guiding strut on infrared signatures of exhaust system, *J. Aerospace Power*, 2020, **35**, (10), pp 2078–2088.
[8] Wang, X., Zhang, J. and Shan, Y. Effects of film hole arrangement on central-cone cooling and infrared radiation characteristics of exhaust system, *J. Aerospace Power*, 2016, **31**, (4), pp 830–835.
[9] Zheng, Q., Xu, Z., Wang, Y., Sun, F. and Zhang, H. Overall optimization design of high temperature components cooling coefficient for lower infrared turbofan engine, *Infrared Phys. Technol.*, 2019, **102**, pp 1–4.
[10] Gao, X., Yang, Q., Zhou, H. and He, J. Numerical simulation on the infrared radiation characteristics of S-shaped nozzles, International Conference on Structural Engineering, Vibration and Aerospace Engineering, 2013, pp 282–286.
[11] Shan, Y., Zhang, J. and Pan, C. Numerical and experimental investigation of infrared radiation characteristics of a turbofan engine exhaust system with film cooling central body, *Aerospace Sci. Technol.*, 2013, **28**, (1), pp 281–288.
[12] Zhou, B. and Ji, H. The effect of plug cooling on infrared radiation characteristic of axisymmetric individual exhaust system, *Infrared Technol.*, 2016, **38**, (5), pp 422–428.
[13] Mattingly, J., Heiser, W. and Daley, D. *Aircraft Engine Design*, Reston, 2015, Virginia, USA.
[14] Saravanamuttoo, H., Rogers, G. and Cohen, H. *Gas Turbine Theory*, 2001, New Jersey, USA.
[15] Walsh, P. *Gas Turbine Performance*, Oxford, UK, 2004.
[16] Hendricks, E. *A Multi-Level Multi-Design Point Approach for Gas Turbine Cycle and Turbine Conceptual Design*, Georgia Institute of Technology, Atlanta, USA, 2017.
[17] Hughes, M., Perullo, C. and Mavris, D. Common core engine design for multiple applications using a concurrent multi-design point approach, 50th AIAA/ASME/SAE/ASEE Joint Propulsion Conference, 2014.
[18] Schutte, J. *Simultaneous Multi-Design Point Approach to Gas Turbine On-Design Cycle Analysis for Aircraft Engines*, Georgia Institute of Technology, Atlanta, USA, 2009.
[19] Schutte, J., Tai, J. and Mavris, D. Multi-design point cycle design incorporation into the environmental design space, 48th AIAA/ASME/SAE/ASEE Joint Propulsion Conference & Exhibit, 2012.
[20] Zheng, H. Construction and application of multi-design point method to perform thermodynamic cycle analysis for aeroengine, *Gas Turbine Exp. Res.*, 2019, **32**, (5), pp 8–14.
[21] Coello, C, and Lechuga, M. MOPSO: a proposal for multiple objective particle swarm optimization, Proceedings of the 2002 Congress on Evolutionary Computation, 2002.
[22] Frank, M., Drikakis, D. and Charissis, V. Machine-learning methods for computational science and engineering, *Computation*, 2020, **8**, (15), pp 1–35.
[23] Damien, S., Vincent, R., Francis, B. and Alexandre, A. Integration methods and optimization algorithms, 31st Conference on Neural Information Processing Systems, Long Beach, CA, USA, 2017.
[24] Kennedy, J. and Eberhart, R. Particle swarm optimization, Proceedings of IEEE international conference on neural network, Piscataway, New Jersey, USA, 1995.

Cite this article: Chen M., Chen H., Zhang H. and Luo J. (2023). Optimisation design of turbofan engine using infrared stealth technology. *The Aeronautical Journal*, **127**, 773–795. https://doi.org/10.1017/aer.2022.88